Mon. Not. R. Astron. Soc. **369,** 1611–1624 (2006) doi:10.1111/j.1365-2966.2006.10480.x

Converging and diverging convection around axisymmetric magnetic flux tubes

G. J. J. Botha,[1⋆] A. M. Rucklidge[1⋆] and N. E. Hurlburt[2⋆]

[1]*Department of Applied Mathematics, University of Leeds, Leeds LS2 9JT*
[2]*Lockheed Martin Solar and Astrophysics Laboratory, Organization L9-41 Building 252, Palo Alto, CA 94304, USA*

Accepted 2006 April 13. Received 2006 April 12; in original form 2006 February 27

ABSTRACT

A numerical model of idealized sunspots and pores is presented, where axisymmetric cylindrical domains are used with aspect ratios (radius versus depth) up to 4. The model contains a compressible plasma with density and temperature gradients simulating the upper layer of the Sun's convection zone. Non-linear magnetohydrodynamic equations are solved numerically and time-dependent solutions are obtained where the magnetic field is pushed to the centre of the domain by convection cells. This central magnetic flux bundle is maintained by an inner convection cell, situated next to it and with a flow such that there is an inflow at the top of the numerical domain towards the flux bundle. For aspect ratio 4, a large inner cell persists in time, but for lower aspect ratios it becomes highly time dependent. For aspect ratios 2 and 3 this inner convection cell is smaller, tends to be situated towards the top of the domain next to the flux bundle, and appears and disappears with time. When it is gone, the neighbouring cell (with an opposite sense of rotation, i.e. outflow at the top) pulls the magnetic field away from the central axis. As this happens a new inner cell forms with an inflow which pushes the magnetic field towards the centre. This suggests that to maintain their form, both pores and sunspots need a neighbouring convection cell with inflow at the top towards the magnetic flux bundle. This convection cell does not have to be at the top of the convection zone and could be underneath the penumbral structure around sunspots. For an aspect ratio of 1, there is not enough space in the numerical domain for magnetic flux and convection to separate. In this case the solution oscillates between two steady states: two dominant convection cells threaded by magnetic field and one dominant cell that pushes magnetic flux towards the central axis.

Key words: convection – MHD – Sun: magnetic fields – sunspots.

1 INTRODUCTION

On the visible surface of the Sun, magnetic flux is pushed to the boundaries of granules and supergranules where they (possibly) grow in field strength to becomes pores. These pores may grow into sunspots, which can have lifetimes of up to several weeks. High-resolution observations have shown that sunspots possess intricate magnetic structures (Sobotka 2003; Thomas & Weiss 2004; Gizon & Birch 2005), the origin and maintenance of which need to be explained.

It is well established that a pore on the Sun is surrounded by a converging surface flow, as well as a downflow next to the magnetic flux tube of the pore (Knölker & Schüssler 1988; Sankarasubramanian & Rimmele 2003). These observations suggest that a pore is surrounded by convection cells with surface flows directed towards the pore – a conclusion supported by numerical simulations (Leka & Steiner 2001). In contrast, sunspots are surrounded by surface flows (the moat cell) that are flowing predominantly away from the spot. Hurlburt & Rucklidge (2000) found in a numerical study of idealized axisymmetric flux tubes in cylinders that a steady collar flow with converging flow at the top of the convection cell is always established. On the occasions when an outflow at the top occurred, the flux tube was torn apart, but inevitably this flow was replaced by a steady inflow at the top that consolidated the magnetic flux tube again. Hurlburt & Rucklidge (2000) speculated that sunspots must also have a collar flow, perhaps hidden underneath the penumbra. Bovelet & Wiehr (2003) measured the horizontal movement of *G*-band bright structures in the penumbra and found that in the inner penumbra they move towards the umbra, while in the outer penumbra both inward and outward motion occur. If these structures are connected to the convection underneath the penumbra, then they would indicate large convection cells underneath the sunspot as predicted

⋆E-mail: gert@maths.leeds.ac.uk (GJJB); A.M.Rucklidge@leeds.ac.uk (AMR); hurlburt@lmsal.com (NEH)

by Hurlburt & Rucklidge (2000). However, other explanations like horizontal movements of magnetic flux tubes (Schlichenmaier 2002) or convection patterns in the penumbral magnetic field (Weiss 2002) are also possible. Helioseismic measurements support the concept of a collar flow that ensures the integrity of the umbral flux tube (Gizon & Birch 2005; Tong 2005). They show that underneath the Evershed flow in the penumbra, there exists a converging flow as well as a downflow up to a depth of approximately 3 Mm. Below these flows there is an outflow that extends to more than 30 Mm from the sunspot axis. Again this result is ambiguous, because the flow does not appear in f-mode measurements, which give only an outflow to a depth of at least 10 Mm, corresponding to the moat flow on the surface (Gizon & Birch 2005).

In this paper the results from Hurlburt & Rucklidge (2000) are confirmed with more realistic parameter values and greater stratification (depth). We obtained time-dependent flows that show a richness in the convection patterns not seen before. For some parameter values, outflows occur at the top of the numerical domain, with small convection cell flowing inwards forming intermittently between the large outflowing convection cell and the flux tube. Our results emphasize that the integrity of a flux bundle needs a surrounding convection cell with inflow at the top (towards the flux bundle).

In order to model some of the observed magnetic phenomena in the photosphere and upper layers of the convection zone, we choose the physical parameters in our model to be as close as possible to their solar values, while taking the constraints imposed by the numerical method and our idealized model into consideration. Most of the convection zone consists of a fully ionized gas, which implies that the plasma behaves almost as an ideal, monatomic gas (Stix 2002). The exception is a thin layer close to the photosphere (with thickness $0.1\,\mathrm{R}_\odot$) where the plasma is partially ionized, but even here the deviation from the equation of state for an ideal gas is less than 1 per cent (Christensen-Dalsgaard 2002). We therefore choose the ratio of specific heats to be that of a monatomic gas $\gamma = 5/3$ throughout our domain. We expect that convective motions will result in a nearly adiabatic plasma in our model and consequently choose the initial stratification, as determined by the polytropic index $m = 1.495$, to be close to its adiabatic value of $m = 1.5$. This choice of m is sufficiently superadiabatic so that buoyancy will allow convection to occur. A large Rayleigh number R is needed to adequately model solar convection: we typically work with $R \sim O(10^5)$. The value of m together with the choice of temperature gradient θ (see equation 1) determines that our model describes a layer in the plasma that has as its top boundary a level that is approximately 500 km beneath the visible surface of the Sun and a bottom boundary at approximately 6000 km (Stix 2002). This implies that we are describing the upper 1 per cent of the solar radius, or equally the upper 2.5 per cent of the convection zone, while excluding the upper boundary layer. The aspect ratio of our numerical domain is never smaller than one, so that the convection described in the model is on the supergranular scale.

The Prandtl number σ is chosen to be small, so that the plasma is thermalized and all temperature perturbations are small. The ratio of magnetic to thermal diffusion ζ is chosen to be small (0.2) at the top of the domain, but due to the density gradient it is $\zeta = 4.38$ at the bottom boundary. Linear theory predicts that $\zeta < 1$ leads to oscillations, while $\zeta > 1$ leads to steady overturning convection (Chandrasekhar 1961). The same behaviour has been confirmed in non-linear numerical calculations (Weiss et al. 1990), where large R values lead to aperiodicity in the oscillatory solutions when $\zeta < 1$. In our model $\zeta = 1$ at a level that is approximately a third of the depth of the domain below the upper boundary.

The analytical model is described in Section 2.1 and its numerical treatment explained in Sections 2.2 and 2.3. The numerical results (Section 3) start with aspect ratio $\Gamma = 4$ and then move progressively to smaller values until $\Gamma = 1$. Only selected illustrative results are presented. They show that for large aspect ratios ($\Gamma = 4$ in Section 3.1), one obtains an anticlockwise convection cell next to the central magnetic flux bundle that is almost time independent. This means there is an inward flow at the top of the numerical domain (close to the solar surface) converging on the flux tube, which is reminiscent of convection around pores on the solar surface. For smaller aspect ratios ($\Gamma = 3$ in Section 3.2 and $\Gamma = 2$ in Section 3.3), the solution becomes highly time dependent, with a smaller anticlockwise convection cell forming and being destroyed in a semiregular manner. In these cases a large permanent clockwise convection cell forms with outflow at the top of the numerical domain, similar to convection around sunspots. For $\Gamma = 1$ the aspect ratio is too small to allow a total separation between magnetic flux and convection, and the final solution oscillates between two states where magnetic flux and convection cells are intertwined. The presentation of the numerical results is followed by their discussion in Section 4, where the work is put in context with previously published results. The paper is concluded with a summary of the main result.

2 MODEL

We solve the partial differential equations (PDEs) that describe compressible magnetoconvection in axisymmetric geometry, using a numerical code developed for this purpose. The PDEs and auxiliary equations are the same as those used by Hurlburt & Rucklidge (2000), where a detailed description of the model can be found.

2.1 Equations

The initial temperature and density profiles in the vertical (z) direction are given by

$$T = T_0(1+\theta z), \qquad \rho = \rho_0(1+\theta z)^m, \tag{1}$$

with the 0 subscript defining the quantity at the top of the box ($z = 0$), θ the initial temperature gradient and m the polytropic index. The PDEs used to solve for fully compressible, non-linear axisymmetric magnetoconvection are

$$\frac{\partial \rho}{\partial t} = -\nabla\cdot(\boldsymbol{v}\rho), \tag{2}$$

$$\frac{\partial \boldsymbol{v}}{\partial t} = -\boldsymbol{v}\cdot\nabla\boldsymbol{v} - \frac{1}{\rho}\nabla P + \theta(m+1)\hat{\boldsymbol{z}} + \frac{\sigma K}{\rho}\left(\nabla^2\boldsymbol{v} + \frac{1}{3}\nabla\nabla\cdot\boldsymbol{v}\right) - \frac{\sigma\zeta_0 K^2 Q}{\rho}\boldsymbol{j}\times\boldsymbol{B}, \tag{3}$$

$$\frac{\partial T}{\partial t} = -\boldsymbol{v}\cdot\nabla T - (\gamma-1)T\nabla\cdot\boldsymbol{v} + \frac{\gamma K}{\rho}\nabla^2 T + \frac{\sigma K(\gamma-1)}{\rho}\left(\frac{1}{2}\boldsymbol{\tau}:\boldsymbol{\tau} + \zeta_0^2 Q K^2 j^2\right), \tag{4}$$

$$\frac{\partial A_\phi}{\partial t} = (\boldsymbol{v}\times\boldsymbol{B})_\phi - \zeta_0 K(\nabla\times\boldsymbol{B})_\phi, \tag{5}$$

with the auxiliary equations

$$P = \rho T, \qquad \boldsymbol{j} = \nabla\times\boldsymbol{B} = \hat{\boldsymbol{\phi}}\, j, \tag{6}$$

$$\nabla \cdot \boldsymbol{B} = 0, \qquad \boldsymbol{B} = \nabla \times (\hat{\phi} A_\phi). \tag{7}$$

Here the notation has its usual meaning, with $\boldsymbol{\tau}$ the rate of strain tensor given by

$$\boldsymbol{\tau} = \begin{bmatrix} 2\,\partial u/\partial r & 0 & \partial u/\partial z + \partial w/\partial r \\ 0 & 2u/r & 0 \\ \partial u/\partial z + \partial w/\partial r & 0 & 2\,\partial w/\partial z \end{bmatrix}, \tag{8}$$

and with γ the ratio of specific heats, σ the Prandtl number, ζ_0 the magnetic diffusivity ratio at $z = 0$, K a dimensionless thermal conductivity and Q the Chandrasekhar number. The Rayleigh number

$$R = \theta^2 (m+1) \left[1 - \frac{(m+1)(\gamma - 1)}{\gamma}\right] \frac{(1+\theta/2)^{2m-1}}{\sigma K^2} \tag{9}$$

is a measure of the importance of buoyancy forces compared to viscous forces in the middle of the layer, and is used to drive the convection in the model. All quantities are dimensionless, with length scaled proportional to the depth of the numerical domain, time scaled proportional to the sound speed at the top of the numerical domain and temperature, magnetic field, density and pressure all scaled to their initial values at the top of the numerical domain.

2.2 Numerical boundaries

The computational domain is a cylinder of radius Γ, so that (r, z) satisfy

$$0 \leqslant r \leqslant \Gamma, \qquad 0 \leqslant z \leqslant 1, \tag{10}$$

with $z = 0$ the top of the box (Fig. 1). We require that all variables be sufficiently well behaved at the axis ($r = 0$) and that the differential operators in the PDEs are non-singular. This implies that

$$\frac{\partial \rho}{\partial r} = u = \frac{\partial w}{\partial r} = A_\phi = B_r = \frac{\partial B_z}{\partial r} = j = \frac{\partial T}{\partial r} = 0, \tag{11}$$

at $r = 0$, where the non-dimensional velocity is given by $\boldsymbol{v} = (u, 0, w)$. Terms like u/r are evaluated using l'Hôpital's rule, while terms like u/r^2 cancel algebraically.

At the bottom of the box ($z = 1$) the temperature is constant and the magnetic field vertical. The bottom boundary is also impenetrable and stress free, i.e.

$$T = 1 + \theta, \qquad \frac{\partial A_\phi}{\partial z} = w = \frac{\partial u}{\partial z} = 0. \tag{12}$$

The outside wall ($r = \Gamma$) is a slippery, perfectly electrically conducting wall with no lateral heat flux across it:

$$A_\phi = \frac{\Gamma}{2}, \qquad \frac{\partial T}{\partial r} = u = \frac{\partial w}{\partial z} = j = 0. \tag{13}$$

The value of A_ϕ is chosen so that the initial vertical uniform field satisfies $B_z = 1$.

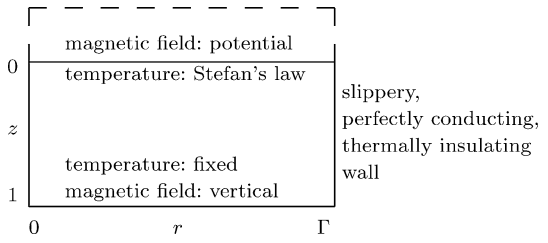

Figure 1. Computational domain $0 \leqslant r \leqslant \Gamma$ and $0 \leqslant z \leqslant 1$, indicating the boundary conditions. At the axis $r = 0$ (left edge of picture) regularity conditions apply.

The top of the box is treated as impenetrable for the plasma, but radiative and potential field boundary conditions are applied to the temperature and magnetic field. Specifically, we set

$$\frac{\partial T}{\partial z} = \theta T^4, \qquad \frac{\partial A_\phi}{\partial z} = M_{\rm pot}(A_\phi), \qquad \frac{\partial u}{\partial z} = w = 0, \tag{14}$$

where $M_{\rm pot}$ is a linear operator matching the potential field to the magnetic field in the domain (that is, the values of B_r and B_z are continuous across the boundary). The potential field is solved by assuming an infinitely tall conducting cylinder of radius Γ above the domain, with the magnetic field becoming uniform as $z \to -\infty$. A more detailed description of the calculation of the potential field is given by Hurlburt & Rucklidge (2000).

The density does not in principle satisfy boundary conditions, but we impose the value of the normal derivative of ρ obtained from the momentum equation (3).

2.3 Numerical method

The numerical code was developed specifically for these types of calculations (Hurlburt & Rucklidge 2000). Sixth-order spatial accuracy is obtained using compact finite differences, with fourth-order temporal accuracy using a modified (explicit) Bulirsch–Stoer integration technique. At the boundaries first-order derivatives are evaluated to fifth-order accuracy and second-order derivatives to fourth-order. The calculations were initiated with a low numerical resolution that still resolved the physics. As the calculations progressed, the resolution was increased to keep the physical processes fully resolved. The grid intervals were chosen to be equal in the two directions. The time-step was limited by the Courant condition (taking the maximum sound and Alfvén speeds, as well as thermal diffusive limits into account), multiplied by a safety factor of 0.5.

3 NUMERICAL RESULTS

Throughout we have used $T_0 = 1$, $\rho_0 = 1$. Unless otherwise stated, the results shown here have been obtained with Rayleigh number $R = 10^5$, $\sigma = 0.1$, $\zeta_0 = 0.2$, $\theta = 10$, $m = 1.495$ and $\gamma = 5/3$. Throughout the paper the results are presented in the format given in Fig. 2.

The numerical code operates with a maximum Mach number $\leqslant$1.8. For most of the numerical runs the final state has a maximum Mach number of approximately 1.5.

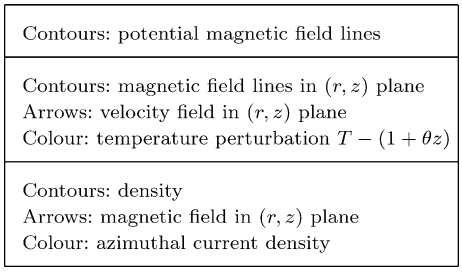

Figure 2. Format of diagnostics for individual numerical solutions. The temperature perturbation in the middle box is colour coded so that blue is cold and red is hot. The azimuthal current in the bottom box is colour coded so that positive values are graded towards red and negative values towards blue. The $r = 0$ axis is on the left.

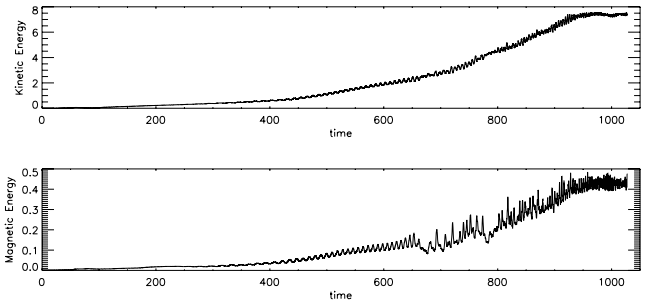

Figure 3. Time evolution of total kinetic and magnetic energy over the duration of a simulation with $\Gamma = 4$ and $Q = 100$, showing a long transient with oscillations before the system settles down at $t \approx 950$.

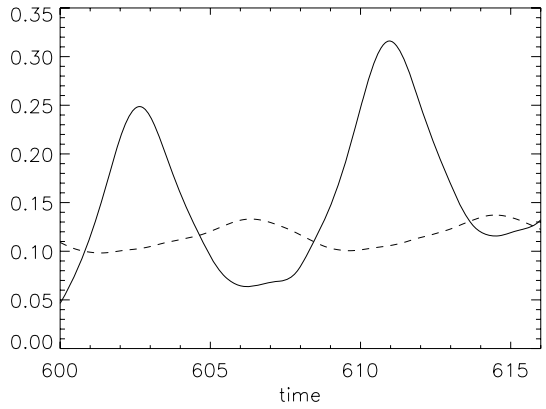

Figure 4. Time evolution of total kinetic energy (solid line) and total magnetic energy (broken line). The time interval is taken from Fig. 3 and contains two cycles of the periodic fluctuations, with the second plotted in Fig. 5. The total kinetic energy was reduced by 1.8 to fit on the same scale.

3.1 Solutions with $\Gamma = 4$

The results shown here were obtained with Chandrasekhar number $Q = 100$ and aspect ratio $\Gamma = 4$.

The time evolution of the total kinetic and magnetic energy is presented in Fig. 3. Soon after initialization a clockwise convection cell forms at the outer (right-hand side) boundary, while the magnetic field is pushed towards the axis (left-hand side) to form a flux tube. The aspect ratio provides enough space for two convection cells to form, with the inner cell (on the left) convecting in an anticlockwise direction, i.e. inflow at the top of the domain. Both convection cells grow with time, which causes the magnetic field to be compressed into a flux bundle on the left-hand side. The convection cells and the flux bundle push against one another, and by doing so create a regular oscillation (Fig. 4) that grows in amplitude as the numerical run progresses. This process can be explained with the help of Fig. 5. When the magnetic field lines are compressed against the left-hand side of the numerical box (Fig. 5a), the total magnetic energy peaks (Fig. 4). At this time the flow velocity in the inner convection cell has just passed its lowest level. The low velocities allow the magnetic field lines to expand into the space occupied by the convection cells, and in doing so they compress the convection cells against the right-hand boundary of the numerical box (Fig. 5b). The expansion of the magnetic field lines lowers the total magnetic energy in the simulation, so that it experiences a minimum when the magnetic field lines are maximally extended (Fig. 5c). The compression of the convection cells causes their flow velocities to increase, which causes the total kinetic energy of the simulation to rise (Fig. 4). The maximum peak in total kinetic energy in Fig. 4 corresponds to a time just after Fig. 5(c), when the convection cells are most compressed and the flow in the simulation most vigorous. The high flow velocities cause the convection cells to increase their size, and in doing so they compress the magnetic field lines against the left-hand boundary (axis) of the numerical domain (Fig. 5d). As this process continues, the convection cells slowly gain size at the expense of the magnetic flux bundle, and both the total kinetic and magnetic energies increase with time, as shown in Fig. 3.

This process continues until time 900, when both the total kinetic and magnetic energies level out. Fig. 6 show the numerical solution after time 900. There is little time dependence in the numerical solution at this stage. A comparison with Fig. 5 shows that the outer cell on the right-hand side has decreased in size, while the inner cell on the left has grown to be the largest feature of the solution. The anticlockwise convection of this cell keeps the magnetic field lines compressed in a bundle on the left-hand side. This steady solution is similar to the results published by Hurlburt & Rucklidge (2000).

3.2 Solutions with $\Gamma = 3$

The results shown here were obtained with $Q = 100$ and aspect ratio $\Gamma = 3$.

Whatever the initial perturbation, the solution quickly establishes a clockwise convection cell at the outer (i.e. right-hand side) boundary, which exists until the simulation is terminated. Initially it grows in size, but quite early during the numerical run (time 180) it reaches maximum size. After that an inner anticlockwise convection cell forms that slowly grows with time. This growth is characterized by a gentle oscillation in total magnetic and kinetic energy (Fig. 7), following the same process as was described in Section 3.1: the magnetic flux bundle and the inner convection cell push against each other, competing for the available space in the numerical domain. As the simulation continues, the convection cell slowly grows in size, the magnetic field lines become more compressed and the amplitude of the oscillations increases. This process continues until time 570 when the oscillation becomes so violent that the inner convection cell is destroyed and reforms during each oscillation cycle. The periodic destruction of the inner convection cell allows the clockwise convection cell on the right-hand side to grow in size, pushing the magnetic field lines towards the axis and thereby increasing the total magnetic and kinetic energy until both reach a saturation level after time 850 (Fig. 7). This oscillation is qualitatively different from the results published by Hurlburt & Rucklidge (2000).

Each cycle, during which the inner convection cell is destroyed and reforms, is characterized by a spike in the total magnetic energy. Fig. 8 shows a time interval from Fig. 7 in more detail and contains two full cycles of the fluctuations. The numerical solution of the first cycle is presented in Fig. 9. A comparison of Figs 8 and 9 shows that the increasing convection of the anticlockwise inner cell provides an impulse that pushes magnetic field lines to the axis (i.e. left-hand side) of the box (Fig. 9b). This action increases first the total kinetic and then the total magnetic energy. As the magnetic field lines move towards the axis, the anticlockwise convection decreases. This lack of anticlockwise convection allows the magnetic field lines to spread to the right, which decreases the total magnetic energy in the system. This process is seen as a spike in the total magnetic energy.

The anticlockwise convection cell also tries to convect the magnetic field lines away from the axis when it is at its strongest. This causes some field lines to move at the bottom of the numerical box to the right of the domain (Fig. 9c), where they are caught in the

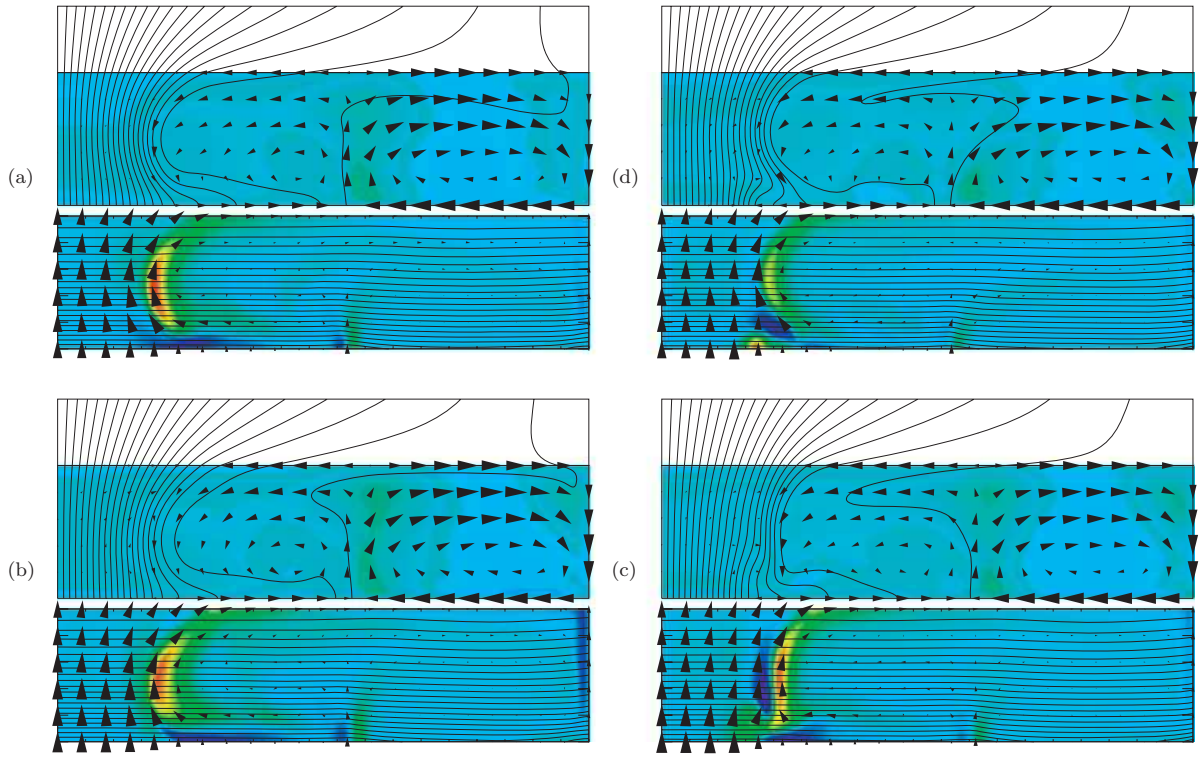

Figure 5. Time evolution with $\Gamma = 4$ and $Q = 100$. The time sequence starts at the top left-hand corner and moves in an anticlockwise direction: (a) $t = 606.9$; (b) $t = 608.4$; (c) $t = 610.8$; (d) $t = 612.3$; with $t = 614.7$ similar to (a). The time evolution of the total kinetic and magnetic energy of this sequence is presented in Fig. 4. The total magnetic energy is highest in (a) while the total kinetic energy is highest in (c). The diagnostics are described in Fig. 2.

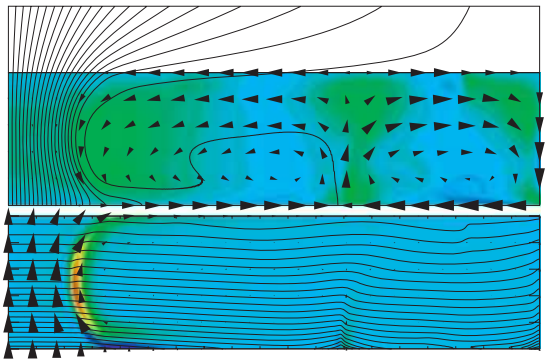

Figure 6. Steady solution at time 990.1 with $\Gamma = 4$ and $Q = 100$.

convection of the larger clockwise cell and are moved upward and outward, i.e. to the right-hand side (Fig. 9d). This movement, together with the reduced strength of the anticlockwise convection, allows the larger clockwise cell to fill the whole box (Fig. 9e) and the total kinetic energy of the solution shows a second (lower) peak (Fig. 8). As soon as the magnetic fields are convected across the top of the numerical domain, another anticlockwise convection cell forms at the top left-hand side of the box (Fig. 9f), decreasing the total kinetic energy. The total kinetic energy rises again only when the strength of the anticlockwise inner convection cell increases and the whole process repeats itself.

Fig. 9(c) shows that as the magnetic field reaches maximum strength on the axis (i.e. left-hand side), a blob of cold plasma moves down the magnetic flux tube, subsequently to be convected to the outer boundary on the right-hand side by the large clockwise convection cell.

When the clockwise convection cell dominates the solution (Figs 9a and f), an outflow occurs at the top boundary of the numerical domain, reminiscent of sunspot behaviour. The correspondence with sunspots is strengthened by the fact that the magnetic field is horizontal close to the surface. However, the outflow pulls magnetic field away from the flux tube and the tube's integrity is maintained only by the formation of an intermittent anticlockwise (inflow) convection cell. By pushing the magnetic field back towards the centre of the numerical domain, the anticlockwise convection destroys the horizontal field at the top boundary (Figs 9c and d) and it only reforms when the clockwise convection starts pulling magnetic field away from the flux tube (Fig. 9e).

At time 675 there is a pause in the spiking of the total magnetic energy (Fig. 7). This is caused by the inner anticlockwise convection cell re-establishing itself for a short while. During this time cold blobs of plasma are convected down the side of the magnetic flux tube, underneath the inner convection cell and over the outer clockwise cell to gather at the lower right-hand corner of the numerical domain. This disruption in the regular rhythm of the fluctuations can happen at any time during the simulation. However, it is always of short duration, with the regular fluctuations re-establishing themselves afterward.

3.3 Solutions with $\Gamma = 2$

The results in this section were obtained with an aspect ratio $\Gamma = 2$ and various magnetic field strengths. Increasing the magnetic field strength through the value of Q has the effect that the solution takes

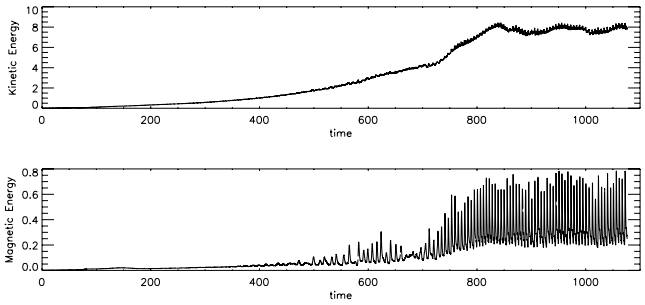

Figure 7. Time evolution of total kinetic and magnetic energy over the duration of a simulation with $\Gamma = 3$ and $Q = 100$.

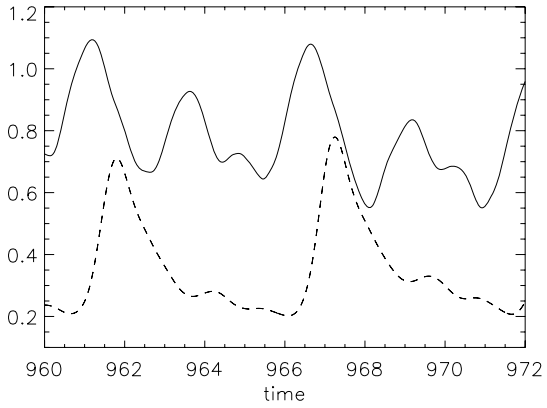

Figure 8. Time evolution of total kinetic energy (solid line) and total magnetic energy (broken line) in the domain. The time interval is taken from Fig. 7 and contains two cycles of the periodic fluctuations, with the first plotted in Fig. 9. The total kinetic energy was reduced by 7.2 to fit on the same scale.

longer to reach its final state, as shown in Fig. 10. The final levels of the total kinetic energy of the solutions are similar, which indicate that the value of Q does not affect the velocities in the convection cells. In contrast, the value of Q influences the radii of the magnetic flux tubes (Hurlburt & Rucklidge 2000).

Fig. 11 shows the time evolution of the total magnetic field during the numerical runs. As the final state is reached, the total magnetic field shows large fluctuations. The lower values of Q show a more random fluctuation pattern, while the higher Q values show the periodic spikes observed in Section 3.2. The detail of one such regular cycle is shown in Fig. 12 for $Q = 100$. When there is an unstable inner convection cell present, the magnetic field strength influences the temporal behaviour of this cell. For low magnetic field strengths the cycle (if it exists) appears to be random, while stronger magnetic fields ($Q \geqslant 40$) bring periodicity to the cycle. This is seen in Figs 11 and 12 as well as in Figs 13–17.

In Figs 13 and 14, the final solutions with $Q = 5$ and 10 are presented. For these low values of magnetic field strengths an inner anticlockwise convection cell forms that changes its shape as it evolves with time, but is not completely destroyed. A consequence of this is that the top boundary between the plasma and the potential magnetic field shows a permanent inflow into the magnetic flux tube, which changes amplitude with time. Cold plasma is convected down the flux tube and gathers at the boundary between the two convection cells. At random stages during the numerical simulation this cold blob of plasma is convected across the top of the outer convection cell to the right-hand corner of the numerical domain. Fig. 13(b) shows such a process in mid progress. By increasing the magnetic field to $Q = 10$ (Fig. 14), the inner convection cell occupies a narrower space but still has an unstable shape. Where the shape changed mostly in width for $Q = 5$ (Fig. 13), here it changes mostly in depth. Fig. 14 shows that there is magnetic flux underneath this inner convection cell that can be considered as part of the flux tube on the left-hand side. The convection of the cold plasma down the flux tube and across the top of the outer clockwise convection cell is still continuing.

In contrast, the solution with $Q = 20$ (Fig. 15) shows an inner convection cell that is randomly destroyed and reforms during the simulation. However, most of the time it is fluctuating in shape in the upper left-hand side of the box, next to the magnetic flux tube and occupying approximately 3/4 of the depth from the top plasma boundary. This means that most of the time there is an inflow at the top plasma boundary (Fig. 15a), with the occasional outflow when the inner cell is destroyed (Fig. 15b). The convection of cold plasma down the flux tube and across the clockwise convection cell is continuing, as in the cases for lower Q values. It is noticeable that prior to the destruction of the inner cell, it reaches maximum width – and depth – before the outer cell convects everything over itself to the right-hand side.

Fig. 16 shows a solution with $Q = 40$. Again the inner cell is confined to the top right-hand corner next to the magnetic flux tube. During most of the simulation it spends its time changing shape in this position. As it grows it pushes against the flux tube, producing the magnetic energy spikes in Fig. 11, but now the spikes are not necessarily associated with the destruction of the cell. Fig. 11 shows that it increases and decreases in size in a reasonably regular periodic manner. This means that for most of the duration of the numerical simulation there is a flow at the top plasma boundary into the magnetic flux tube. As with $Q = 20$ in Fig. 15(a), it is only when it reaches maximum size in depth that it is destroyed by the clockwise convection cell. When it grows in depth, it pushes down into the magnetic flux tube, parting the magnetic field lines at the bottom (Fig. 16a). An interesting phenomenon that shows here for the first time is that inside the flux tube the horizontal flow along the top plasma boundary is always in the opposite direction of what is happening just outside the magnetic flux tube, irrespective if the outside flow is caused by the inner cell or the larger clockwise convection cell.

For comparison with aspect ratio $\Gamma = 3$ in Fig. 9, numerical results with $Q = 100$ are presented in Fig. 17. For this magnetic field strength the regular pattern of destruction and reformation of the inner cell has established itself, as is shown by the spiking of the total magnetic energy in Fig. 11. However, whereas the inner cell forms next to the flux tube for $\Gamma = 3$, here it forms inside the flux tube (Fig. 17b) and pushes the field lines apart when it grows in size. As a result, at maximum size the inner cell only pushes the field lines apart at the bottom boundary (Fig. 17c), while for $\Gamma = 3$, the bottom field lines are convected upwards by the clockwise convection cell (Figs 9c and d). As in Fig. 16 for $Q = 40$, there is a flow inside the magnetic flux tube along the top plasma boundary, that is always in the counter direction to what is happening just outside the flux tube.

Fig. 12 shows that during each cycle the total kinetic energy peaks twice while the total magnetic energy peaks only once. The magnetic energy peaks when the anticlockwise convection cell is forming and pushing the magnetic field lines together on the axis (Fig. 17c). The total kinetic energy peaks at first when the larger clockwise convection cell dominates the solution and magnetic field lines move away from the axis on the left (Fig. 17a), and a second time when the smaller anticlockwise convection cell has reached its

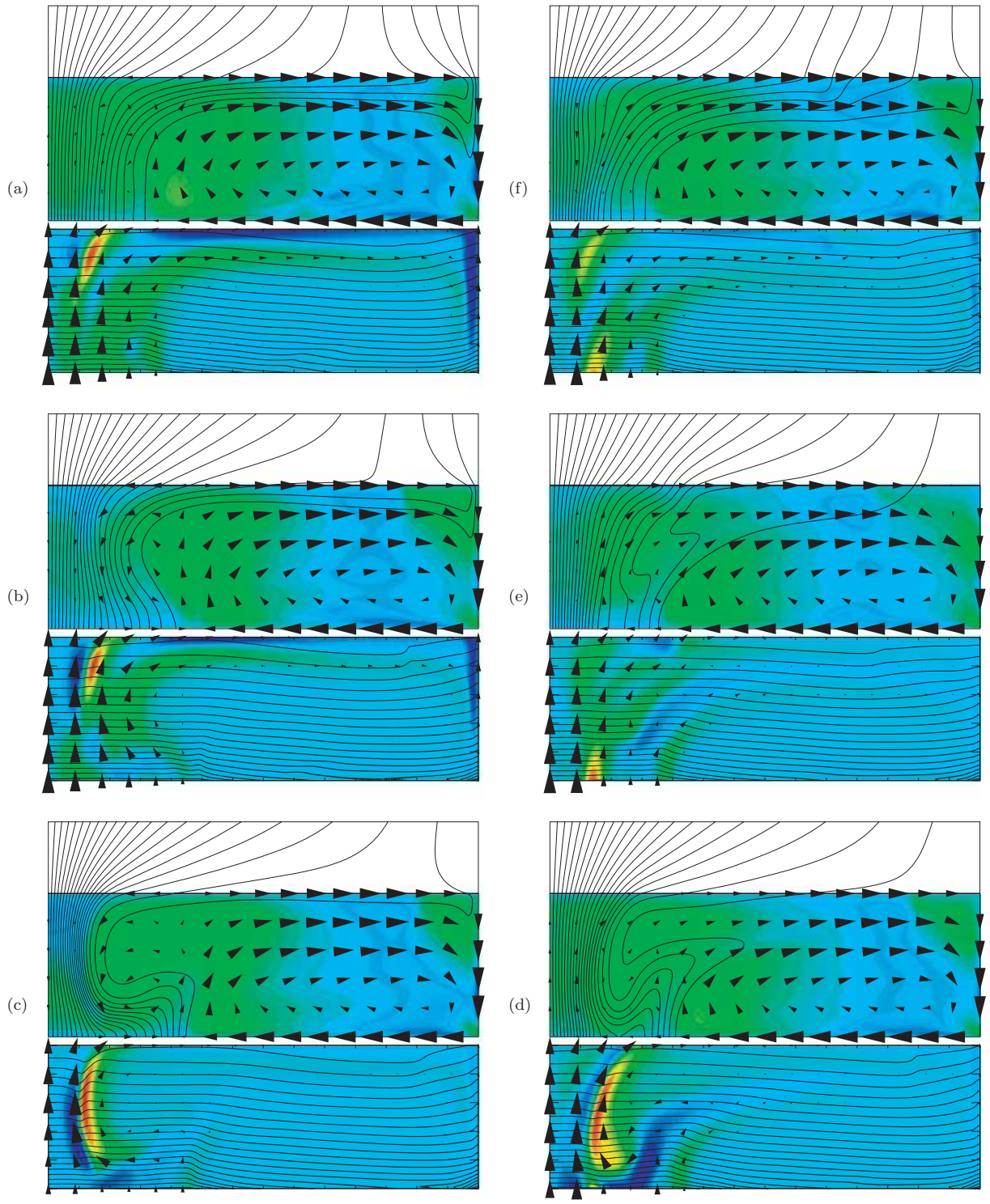

Figure 9. Time evolution with $\Gamma = 3$ and $Q = 100$. The time sequence starts at the top left-hand corner and moves in an anticlockwise direction: (a) $t = 960$; (b) $t = 960.8$; (c) $t = 961.7$; (d) $t = 962.7$; (e) $t = 963.6$; (f) $t = 964.6$; with $t = 965.6$ similar to (a). The time evolution of the total kinetic and magnetic energy of this sequence is presented in Fig. 8. The total magnetic energy has its highest value in (c). The total kinetic energy has its highest value in (b) and its second highest peak in (e).

maximum size between the magnetic field lines and the field lines start to push away from the central axis (Fig. 17c).

As in the case for $\Gamma = 3$ in Section 3.2, the magnetic field forms a horizontal layer at the top of the numerical domain when the clockwise convection cell dominates (i.e. when there is outflow at the top of the box). This is clearly shown in Fig. 16(b) for $Q = 40$ and Fig. 17(a) for $Q = 100$. The outflow also drags magnetic field away from the flux bundle and it is only when an anticlockwise convection cell forms (with inflow at the top boundary) that the flux bundle's integrity is restored. This inflow, however, also tends to destroy

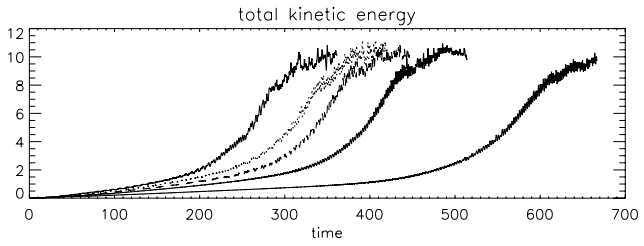

Figure 10. Time evolution of total kinetic energy for $\Gamma = 2$ and different magnetic field strengths. The left-most solid line that levels out at time 340 is $Q = 5$; the dotted line is $Q = 10$; the dashed line is $Q = 20$; the dot–dashed line is $Q = 40$ and the right-most solid line that levels out at time 660 is $Q = 100$.

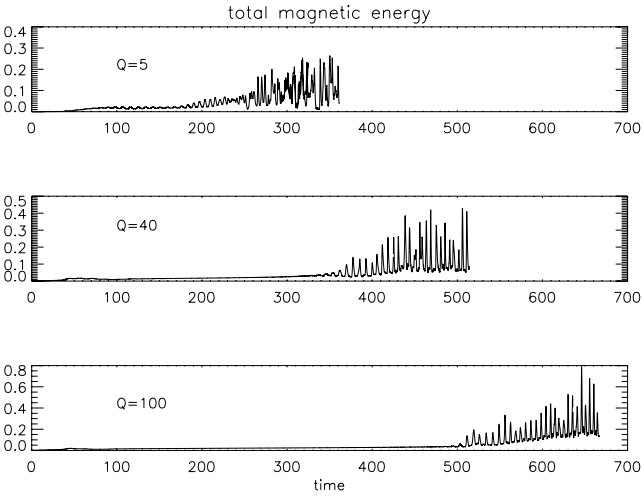

Figure 11. Time evolution of total magnetic energy with $\Gamma = 2$ and magnetic field strengths $Q = 5$, 40 and 100.

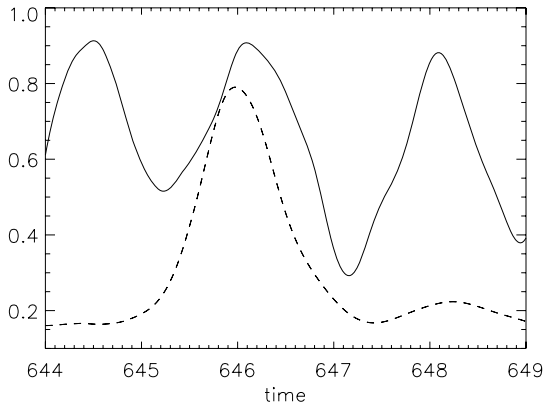

Figure 12. Time evolution of total kinetic (solid line) and magnetic energy (broken line) over the duration of a simulation with $\Gamma = 2$ and $Q = 100$. The time interval is taken from Figs 10 and 11 and contains one cycle which is plotted in Fig. 17. In order to compare the two energies, the total kinetic energy was scaled by subtracting 8.7 from it.

the horizontal magnetic field that exists at the top of the numerical domain, as shown in Fig. 16(a) for $Q = 40$ and Fig. 17(c) for $Q = 100$. When an anticlockwise convection cell resides permanently next to the magnetic flux bundle, it prevents horizontal magnetic field from forming at the top boundary (Figs 13 and 14) even when this anticlockwise cell fluctuates randomly with time, as is the case when $Q = 5$ and 10.

3.4 Solutions with $\Gamma = 1$

The numerical results presented in this section were obtained with Chandrasekhar number $Q = 40$ and aspect ratio $\Gamma = 1$.

The small aspect ratio does not allow enough space for steady convection cells to form separated from the magnetic field. Instead, two final states form and the numerical solution oscillates between these states. The first state is given in Fig. 18 (time 338): two convection cells form in the numerical domain. The smaller is a clockwise cell on the right, while a larger anticlockwise cell forms on the left and bottom of the box. The larger cell forms in the inner region where the magnetic field is the strongest. The second state is given in Fig. 18 (time 360): a large anticlockwise cell forms which pushes the magnetic field towards the axis (left-hand side of the numerical domain). A small remnant of the clockwise convection cell is visible next to the outer boundary on the right-hand side of the domain.

Unlike the growing stages of solutions with $\Gamma = 3$ and 4, the total kinetic and magnetic energy of this final solution oscillate in phase under these conditions (Fig. 19). Both maxima are obtained when the large anticlockwise convection cell dominates the numerical domain. The oscillation loses its regularity if the Chandrasekhar number Q is chosen with smaller values (i.e. a weaker magnetic field), but it keeps going. The lowest value used was $Q = 5$. It is only with a stronger magnetic field (higher Q values) when the oscillation disappears and the solution settles into one final state: the large anticlockwise convection cell, shown in Fig. 18 at time 360.

4 DISCUSSION

4.1 Robustness of results

Another set of numerical results was obtained with Rayleigh number $R = 10^6$, polytropic index $m = 1.45$, Prandtl number $\sigma = 0.1$, together with Chandrasekhar number Q, magnetic diffusivity ratio ζ_0 and aspect ratio Γ given in Table 1. Different boundary values at the top of the numerical domain were used from what are described in this paper (Fig. 1). For these runs the top magnetic field was vertical with no potential field, and the temperature at the top boundary was constant.

The same trends are observed as were described in Section 3 and by Hurlburt & Rucklidge (2000). The width of the magnetic tube in the middle of the axisymmetric cylinder increases with an increase in the value of Q. The number of convection cells fitting into the numerical domain arrange themselves so that the inside cell is always anticlockwise, holding the inside magnetic tube together. When the values of the Chandrasekhar number Q and the aspect ratio Γ combine to allow for a convection area in the numerical domain that is of such a size that only one large clockwise convection cell forms, then there is always a small anticlockwise cell forming at the top right-hand side of the convection area against the magnetic tube, which undergoes cyclic destruction and reformation, as described in Sections 3.2 and 3.3 for aspect ratios $\Gamma = 3$ and 2 in this paper.

A series of numerical runs were performed with a constant temperature and vertical magnetic field with no potential field as the top boundary conditions, and with higher Prandtl numbers. The rest of the parameters were as described in Section 3. For $\sigma = 0.5$ the momentum diffusivity reduces the vigour of the convection. In this case a magnetic flux bundle forms at the central axis with a neighbouring large stable anticlockwise cell with inflow at the top of the domain. When $\sigma = 0.3$ the same results were obtained as described

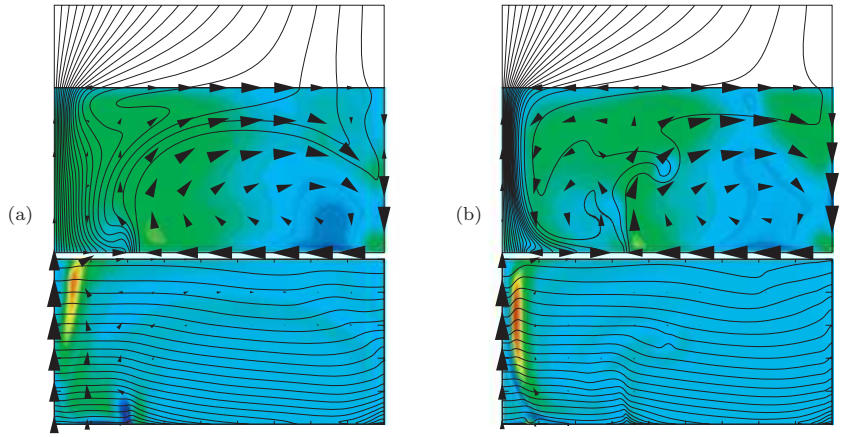

Figure 13. Solutions with $\Gamma = 2$ and $Q = 5$, taken at times (a) $t = 316.2$ and (b) $t = 373.7$. The inner convection cell fluctuates randomly and never disappears completely. Cold blobs of plasma are carried down the side of the flux tube by the inner cell (a) and then over the top of the outer clockwise convection cell (b).

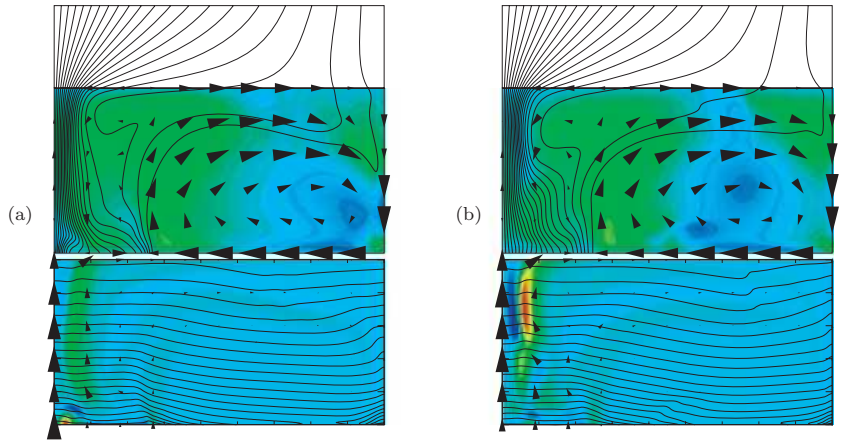

Figure 14. Solutions with $\Gamma = 2$ and $Q = 10$, taken at times (a) $t = 408.6$ and (b) $t = 409.9$. The inner anticlockwise convection cell still persists but varies in depth.

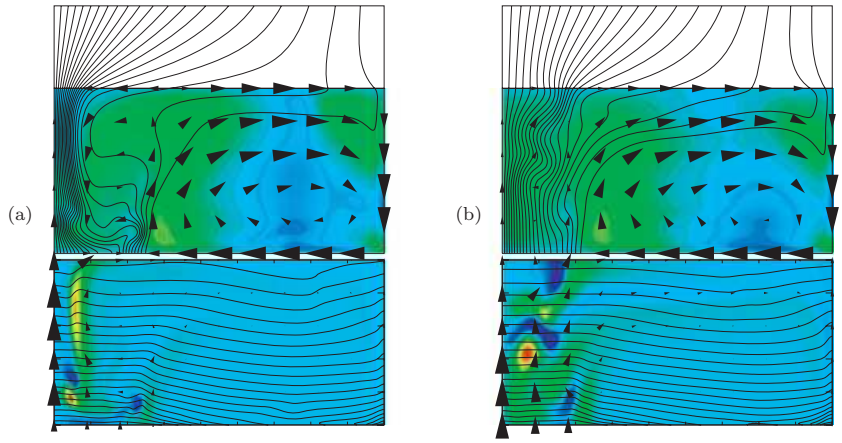

Figure 15. Solutions with $\Gamma = 2$ and $Q = 20$, taken at times (a) $t = 435.8$ and (b) $t = 438.4$. The inner anticlockwise convection cell (a) forms and (b) is randomly destroyed by the large clockwise convection cell.

by this paper. A Prandtl number of $\sigma = 0.1$ often allowed shocks to form at the top boundary, which terminated the numerical runs. Shocks were prevented by changing the top magnetic boundary to match a potential field. (See Section 4.6.)

4.2 Initial energy increase

During the numerical simulations the total kinetic and magnetic energy grow for a long time before they reach a final steady level

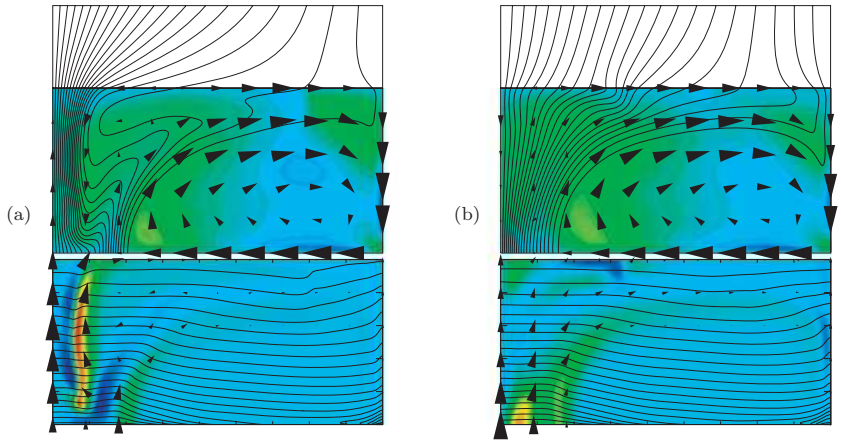

Figure 16. Solutions with $\Gamma = 2$ and $Q = 40$, taken at times (a) $t = 511.9$ and (b) $t = 513.9$. The inner convection cell manages to fracture the magnetic flux tube in (a). A top flow inside the flux tube forms that is always opposite to the flow just outside the tube.

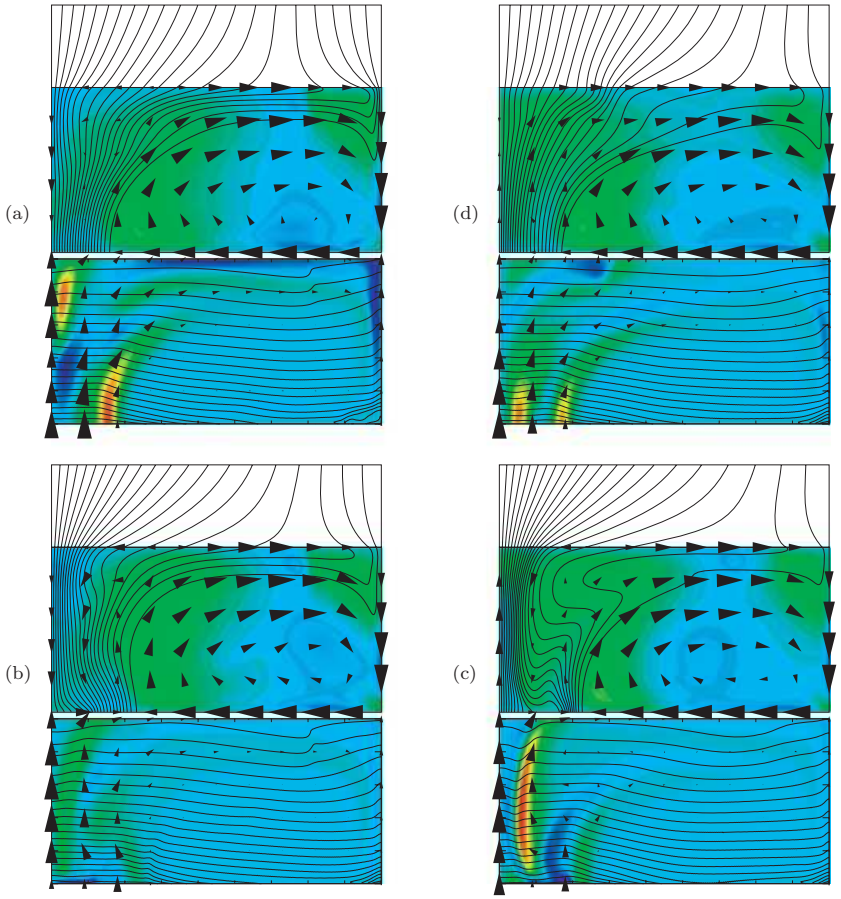

Figure 17. Time evolution with $\Gamma = 2$ and $Q = 100$. The time sequence starts at the top left-hand corner and moves in an anticlockwise direction: (a) $t = 644.1$; (b) $t = 645.2$; (c) $t = 646.3$; (d) $t = 647.6$; with $t = 649$ similar to (a). The time evolution of the total kinetic and magnetic energy of this sequence is presented in Fig. 12. The total magnetic energy is highest in (c), while the total kinetic energy has two peaks: in (a) when the large clockwise convection cell dominates and (c) when the inner anticlockwise convection cell has reached its maximum size.

(Figs 3, 7, 10 and 11). A similar phenomenon was observed in numerical studies of axisymmetric Bénard convection in a cylinder, where a Boussinesq fluid with very small Prandtl numbers accelerated until friction was eventually sufficient to maintain equilibrium (Jones, Moore & Weiss 1976). In our simulations $\zeta_0 = 0.2$ and $\sigma = 0.1$, so that the magnetic diffusivity at the top of the domain and the viscosity are of the same order and both are an order of magnitude smaller than the thermal conductivity.

When the value of Q increases in the simulation, the simulation takes longer to reach its final state (Figs 10 and 11). The increase

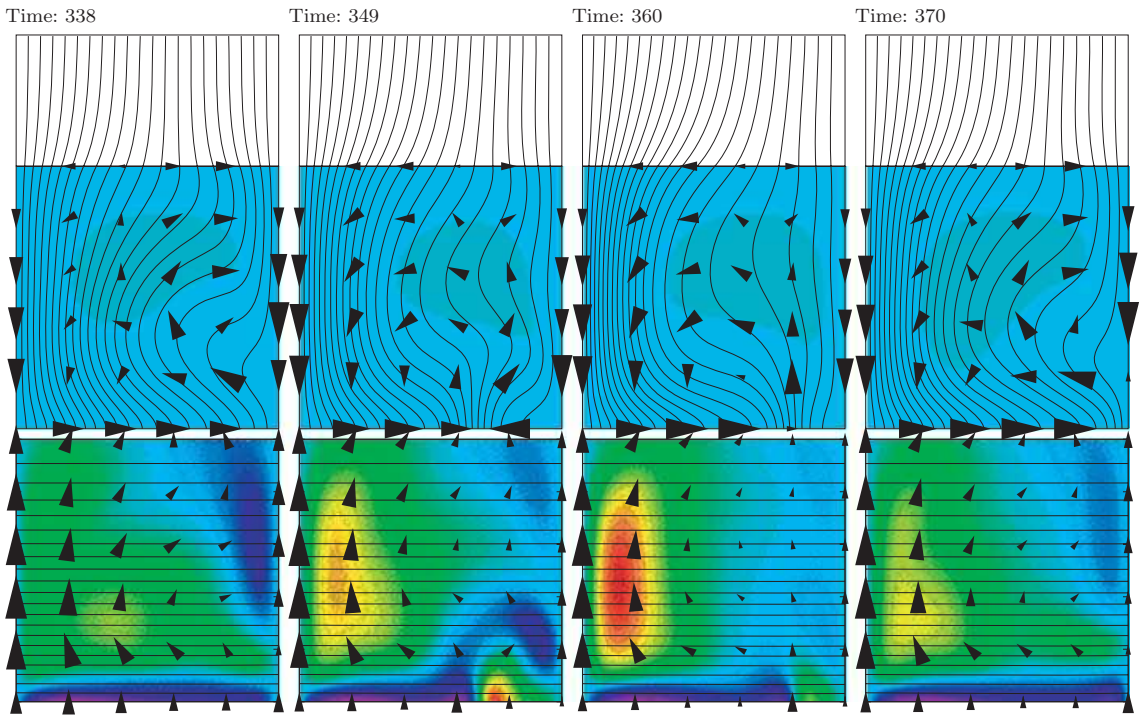

Figure 18. Time evolution with $\Gamma = 1$ and $Q = 40$. At time 338 the inner and outer cells split the domain diagonally. The inner cell grows (time 349) to dominate the numerical domain (time 360), after which the outer cell grows again (time 370). The time evolution of the total kinetic and magnetic energy of this sequence is included in Fig. 19. At time 360 both energies reach their maximum values.

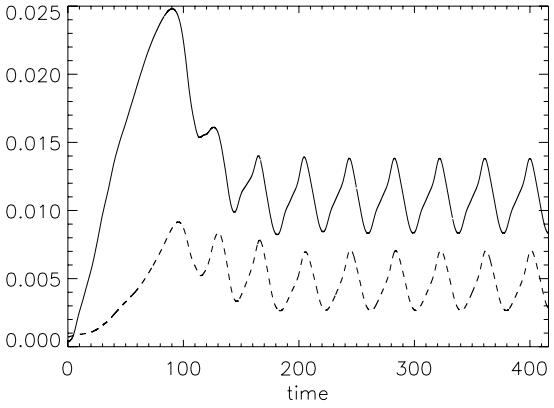

Figure 19. Time evolution of total kinetic (solid line) and magnetic energy (broken line) over the duration of a simulation with $\Gamma = 1$ and $Q = 40$. In order to compare the two energies, the total kinetic energy was scaled by dividing it by 10.

Table 1. Parameter values with $R = 10^6$, $m = 1.45$, $\sigma = 0.1$.

Q	ζ_0	Γ	Q	ζ_0	Γ
10	0.2	4	10^3	0.2	2
100	0.2	2	3×10^3	0.2	2
100	0.2	3	5×10^3	0.2	2
100	0.2	4	7×10^3	0.2	2
300	0.2	2	10^4	0.02	2
300	0.2	3	10^4	0.2	2
300	0.2	4	5×10^4	0.02	2
500	0.2	2	7×10^4	0.02	2
500	0.2	3	8×10^4	0.02	2
500	0.2	4	8×10^4	0.2	2
700	0.2	2	9×10^4	0.02	2
700	0.2	3	10^5	0.2	2
700	0.2	4	10^6	0.02	2

in Q has no effect on the final value of the total kinetic energy (Fig. 10), but as expected the value of the total magnetic energy increases (Fig. 11). The Chandrasekhar number Q is a measure of the strength of the restraining forces in magnetoconvection. By increasing Q the thermal driving forces (represented by the Rayleigh number R) experience more resistance and the the simulation takes longer to reach optimum velocity, when friction is large enough to keep the numerical solution at an equilibrium state.

Another parameter that has a large influence on the levels of total kinetic and magnetic energy and the time it takes to reach these levels is the aspect ratio Γ. As Γ increases, the final value of the total magnetic energy increases because more magnetic flux threads through the numerical domain (if Q stays the same size). The opposite effect on the total kinetic energy is observed: an increase in Γ decreases the vigour of convection and the final levels of the total kinetic energy are lower. The time at which these final energy values are reached also increases with an increase in Γ. These observations point to the influence of the outside wall (Fig. 1) on the physics and suggest care should be taken when comparing these results with solar observations.

4.3 Anticlockwise inner convection cell

In all the simulations an anticlockwise inner convection cell forms. For aspect ratio $\Gamma = 1$ (Section 3.4) the solution oscillates between

a dominant anticlockwise convection cell and a second state where two cells form, the inner cell being anticlockwise. When $\Gamma = 2$ and 3 (Sections 3.3 and 3.2) the inner cell is destroyed and reforms repeatedly. While it exists it is always convecting in an anticlockwise direction. For $\Gamma \geqslant 4$ (Section 3.1) the anticlockwise inner cell is a steady feature of the solution.

Local helioseismic measurements show the existence of converging large-scale surface flows around active complexes of magnetic activity and diverging flows below 10 Mm (Gizon 2004), which should be distinguished from the local flows associated with sunspots. These large-scale flows appear to form toroidal cells when averaged over time-scales longer than a week. The physical argument for the existence of inward flows at the top of the numerical domain in our calculations relies on two observations. The first is that with convection suppressed inside the flux tube, it will be cooler at the top than the outside regions surrounding it. As a result there will be horizontal temperature gradients that will tend to drive flows inwards. The second reason is that the compressibility of the gas means that cold, dense downflows generated at the top close to the cooler flux tube will dominate warm diffuse upflows.

The effect of this anticlockwise inner convection can be seen when the cell is destroyed during runs with $\Gamma = 2$ (Fig. 17) and $\Gamma = 3$ (Fig. 9). While the anticlockwise convection cell exists the magnetic field is confined to the central axis to form a flux tube. As soon as the inner cell is destroyed, the magnetic fields are swept out in a radial direction by the clockwise convection that now exists next to the flux tube. This continues until the anticlockwise cell reforms and starts pushing the magnetic field towards the central axis.

The cycle of formation and destruction of the inner cell is marked by a peak in the total magnetic energy of the solution (Figs 7 and 11). By looking at the time interval between two consecutive peaks ($\triangle t$) one can determine the regularity of this cycle. Fig. 20 shows the $\triangle t$ in Fig. 7 for $\Gamma = 3$ after time 800, when the cycle has fully established itself. Although the $\triangle t$ is not constant, its values span a narrow interval.

The size of the inner convection cell is highly time dependent for aspect ratios $\Gamma \leqslant 3$. For $\Gamma = 2$ the inner cell is situated most of the time in the upper right-hand corner of the numerical domain (Figs 13–17), which is sufficient for the magnetic flux bundle to be maintained at the centre. Table 2 shows the aspect ratios for the inner anticlockwise convection cells, taken as the relation between its maximum width and maximum depth. It shows that the size of the inner cell is less important than the fact that it is convecting in an anticlockwise direction.

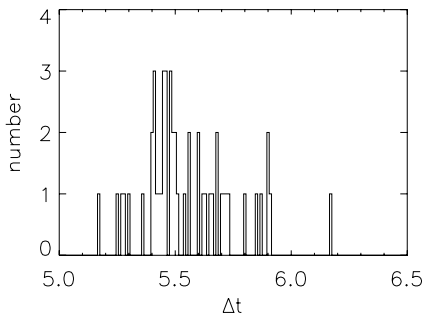

Figure 20. Time intervals between peaks of the total magnetic energy for aspect ratio $\Gamma = 3$ and Chandrasekhar number $Q = 100$. This distribution was sampled from Fig. 7, starting at time 800 until the end of the numerical run.

Table 2. Aspect ratio Γ of inner cell at maximum size.

Box Γ	Q	Max[inner cell Γ]
1	40	0.71
2	5	0.59
2	10	0.41
2	20	0.41
2	40	0.41
2	100	0.41
3	100	0.63
4	100	1.90

4.4 Aspect ratio $\Gamma = 1$

A similar model was used by Cameron & Galloway (2005) to investigate magnetohydrodynamic flows in an axisymmetric tube with $\Gamma = 1$. The differences are a top magnetic boundary condition that was vertical instead of a potential field, and a different parameter regime was investigated. They used $m = 0.05$ which gives a small equilibrium density stratification. By varying θ between 0.1 and 12.9 they obtained from an almost Boussinesq (where m and $\theta \ll 1$) to a fully compressible plasma. In contrast, results are presented in Section 3.4 for a large equilibrium density stratification ($m = 1.495$). All other parameters are comparable, with $\theta = 10$ used in Section 3 as the temperature gradient between top and bottom boundaries. Cameron & Galloway obtained a steady solution for all the parameter values they investigated, with a flux tube at $r = 0$ and a convection cell next to it, similar to Fig. 18 (time 360). In the Boussinesq limit they found no preference between upflow or downflow next to the central flux tube, as expected from the up–down symmetry in this approximation. When the temperature stratification (θ) was increased, they found an increase in the preference for upflow next to the flux tube in the end state. This is in contrast to Section 3.4 which oscillates between two final states for low Q values, while for high Q values one convection cell forms that always has a downflow next to the flux tube.

A comprehensive investigation of a Boussinesq fluid in an axisymmetric cylinder with $\Gamma = 4/3$ was done by Galloway & Moore (1979). For very low Q values a narrow intense flux tube forms at $r = 0$ with a convection cell in the rest of the domain. By increasing Q the flux tube radius increases with all motion inside the flux tube suppressed at first, and then the broad radius starts oscillating as it is pushed by the (still unaffected) convection cell, as in Sections 3.1–3.3 while the plasma is evolving to its final solution. However, unlike the solutions presented here, the total kinetic and magnetic energy oscillate in phase, similar to Fig. 19. The convection direction is allowed equally, depending only on the direction of the initial perturbation. For large Q values the separation between flux tube and convection cell depends on the initialization of the numerical domain: if initialized with a strong flux tube the solution kept this configuration. Also, for large Q the flux tube shows small oscillations, combined with bursts (at longer intervals) during which the flux temporarily increases and the direction of the convection cell reverses, indicating a possible relaxation of the plasma state similar to Sections 3.2 and 3.3. For large Q values the total kinetic and magnetic energy oscillations become out of phase, reminiscent of Fig. 4 which was measured during the growing oscillations for $\Gamma = 4$. That no preference to the convection direction is given, as well as the existence of an oscillating convection direction at large Q values, agrees with the up–down symmetry of the

Boussinesq approximation. A similar pattern of behaviour was found for a Boussinesq plasma in two-dimensional (2D) Cartesian geometry with $\Gamma = 1$ (Proctor & Weiss 1982).

4.5 Magnetic field strength

Increasing the magnetic field strength through the value of Q has the effect that the solution takes longer to reach its final state (Fig. 10), but the level at which the total kinetic energy saturates is not affected by the value of Q. This is true for all aspect ratios as long as the size of the magnetic flux tube (compared to the area of the numerical domain) is not so large as to suppress convection, which is the case when $\Gamma = 1$.

When there is an unstable inner convection cell present, this anticlockwise cell forms and is destroyed repeatedly. For low magnetic field strengths the cycle appears to be random, while stronger magnetic fields bring periodicity to the cycle, as is shown in Figs 11 and 13–17. Once the regular cycle is established, an increase in the magnetic field strength does not affect it. This behaviour is only true for unstable inner convection cells. The magnetic field strength does not affect the behaviour of inner cells that do not show much change over time, as is the case for aspect ratio $\Gamma = 4$.

For solutions with time-independent magnetic flux tubes and convection cells, an increase in Q will increase the width of the tube (Hurlburt & Rucklidge 2000). The time-dependent solutions presented here show that the width of the magnetic tubes is directly related to its neighbouring convection cell. Anticlockwise cells push the magnetic field lines together and the tube width decreases dramatically, while the opposite is true for clockwise convection cells. (See Fig. 9 for aspect ratio $\Gamma = 3$.) However, for low Q numbers the anticlockwise convection is able to press the magnetic field into a much smaller radius than is the case for higher Q values. This is seen for aspect ratio $\Gamma = 2$ when the minimum radius for $Q = 5$ (Fig. 13b) is compared with the minimum radius for $Q = 100$ (Fig. 17c).

Hurlburt & Rucklidge (2000) have shown that the magnetic field strength inside a steady flux tube is independent of the tube's width. In the cases presented here, the magnetic field strength inside the tube is determined by the strength, size and direction of the convection cell next to the magnetic flux tube, provided the domain size is large enough to allow unfettered convection outside the flux tube. Magnetic field increases in strength when an anticlockwise convection cell pushes magnetic field lines towards the axis, and decreases when they are convected away from the axis by a clockwise cell. Because of the time-dependent nature of the convection cells, the magnetic field strength inside the flux tubes is not uniform along the depth (or z direction) of the numerical domain at any given instant of time, as can be seen in Fig. 9 for $\Gamma = 3$ and Figs 13–17 for $\Gamma = 2$.

Sections 3.2 and 3.3 show that when a convection cell with outflow at the top boundary is established next to the magnetic flux bundle, horizontal field lines form a layer at the top of the box. It is known that horizontal field encourages magnetoconvection in the form of convective roles parallel to the field (Weiss 2002). In the present model this is not possible due to the axisymmetry of the numerical model. As the anticlockwise cell reforms next to the magnetic flux tube, the inflow at the top boundary due to the reforming cell pushes all magnetic flux towards the central axis. This happens before enough horizontal field reaches the outer numerical boundary to demonstrate downward flux pumping (Weiss et al. 2004). If one assumes that the outer wall has a similar effect as a counter rotating convection cell, then some suggestion of magnetic flux pumping can be observed in Figs 9(a) and 17(a), where the downflow next to the outer boundary starts to drag the magnetic field with it.

4.6 The influence of the numerical boundaries

The aspect ratio Γ has a huge influence on the type of solution obtained with the numerical code, as seen in Section 3. The outside wall (Fig. 1) was designed to have the least possible influence on the numerical results. Its presence is felt through the radius of the cylinder, with large values of Γ allowing many convection cells to form while small Γ values force the magnetic field and convection to interact in a time-dependent manner. Also, as discussed in Section 4.2, the proximity of the outside wall to the central axis has an influence on the level of convection in the numerical solution.

It is mentioned at the start of Section 3 that the code operates with maximum Mach numbers $\leqslant 1.8$. Because of the temperature profile, the sound speed $c_s = \sqrt{\gamma T}$ is lowest at the top, which allows shocks to form where the top outflow approaches its first obstacle: be it the outside wall (Section 3) or an anticlockwise convection cell ($\Gamma > 4$). When the top magnetic field boundary is vertical with no potential field, shock formation can be limited by raising the value of the Prandtl number to $\sigma = 0.3$, as discussed in Section 4.1. However, for a potential field as the top magnetic boundary, no shocks formed for $\sigma = 0.1$.

The fact that for $\Gamma = 2$ the destruction of the inner anticlockwise convection cell seems to be triggered when the cell grows vertically and touches the bottom boundary (Figs 15 and 16) seems suspicious. The constant temperature at the bottom boundary forms an impenetrable layer for the colder downward convection and one cannot rule out the possibility that the time dependence in the numerical results is partly due to the shallowness of the domain.

The severe boundary conditions of the numerical model limit any direct comparison between these results and sunspot observations, and relaxing them may change the nature of our solution. This suspicion is strengthened by a sunspot model (Schüssler & Rempel 2005) that evolves a series of static equilibria under the influence of a prescribed inflow at the bottom boundary and radiative cooling at the top. In this model magnetic flux disconnects from its magnetic roots between 2 and 6 Mm – a depth within our numerical domain as determined by the chosen parameter values.

5 SUMMARY AND CONCLUSIONS

Axisymmetric simulations are presented for a fully compressible plasma described by the MHD equations. The results of Hurlburt & Rucklidge (2000) are extended by choosing more realistic physical parameters in the model, in order to represent the upper layer of the solar convection zone. As such, these results have implications in the understanding of the formation and maintenance of pores and sunspots.

When the aspect ratio Γ of the cylindrical domain is large enough to allow separation of flux and convection, a magnetic flux bundle forms on the axis that is kept in place by a convection cell with an inflow at the top domain boundary. For $\Gamma = 4$ this inner convection cell is the largest feature of the solution and time independent. As the aspect ratio decreases ($\Gamma = 3$ and 2) the inner cell is smaller and becomes highly time dependent. A cycle of formation and destruction of the inner cell forms, with magnetic flux pushed to the cylindrical axis when the cell forms and flux dispersing into the domain as the inner cell is destroyed. As a result the total magnetic

energy in the domain peaks when the cell forms and is a minimum when the cell is destroyed. For $\Gamma = 2$ a series of numerical runs were performed with lower initial (uniform) magnetic flux. These runs show inner cells that are highly time dependent, deforming but never being destroyed. Only higher initial magnetic flux allows the semiperiodic cycle to form. An aspect ratio of $\Gamma = 1$ does not allow enough space for separation of flux and convection. Two final states form with the solution oscillating between them: a single cell with inflow at the top that pushes magnetic flux to the axis; and two cells with an inner cell with inflow at the top and an outer cell in the opposite direction, with both cells threaded by magnetic flux.

A convection cell forming next to the magnetic flux bundle with a sense of flow such that there is an outflow at the top of the numerical domain tends to drag the magnetic bundle out into a horizontal field. In a three-dimensional (3D) non-axisymmetric model one would expect convection rolls to form that are aligned with the magnetic field (Tildesley & Weiss 2004), suggestive of the penumbral structure. Yet the integrity of the magnetic flux tube in the model is only maintained by a convection cell with a converging flow at its top. These contradicting requirements would suggest that a (perhaps intermittent) convection cell providing an inflow is necessary for maintaining a sunspot. This inflowing cell must be located underneath the penumbral structure, which in turn relies on an outflow for its formation.

The results in this paper are suggestive of how the transition from a pore to a sunspot might work and provide numerical evidence to support the ideas of flux pumping (Weiss et al. 2004) as well as helioseismic measurements (Gizon & Birch 2005). The transition from pore to sunspot in the model is associated with two processes. The first is a decreasing aspect ratio Γ with all other parameters constant (and hence a decreasing of total magnetic flux), which is opposite to the solar case and possibly an artefact of the outer boundary. The second is by increasing the magnetic flux through the Chandrasekhar number Q (again with all other parameters constant), as was shown in Section 3.3 and which is more in agreement with observations.

In conclusion, these numerical runs show that in an axisymmetric cylinder a central magnetic flux bundle forms that relies on a neighbouring convection cell for its maintenance. The convection direction of this cell is such that there is converging flow at its top.

The next stage in the project will be to include the full 3D cylindrical geometry and to investigate the linear stability of these axisymmetric solutions, as well as their non-linear evolution. Preliminary results are described in Hurlburt, Matthews & Rucklidge (2000). Tildesley & Weiss (2004) examined a related linear stability problem in Cartesian geometry using the Boussinesq approximation.

ACKNOWLEDGMENTS

We wish to thank Nigel Weiss for fruitful discussions. GJJB would like to acknowledge the support of PPARC grant number PPA/G/O/2002/00014.

REFERENCES

Bovelet B., Wiehr E., 2003, A&A, 412, 249
Cameron R., Galloway D., 2005, MNRAS, 358, 1025
Chandrasekhar S., 1961, Hydrodynamic and Hydromagnetic Stability. Clarendon Press, Oxford
Christensen-Dalsgaard J., 2002, Rev. Mod. Phys., 74, 1073
Galloway D. J., Moore D. R., 1979, Geophys. Astrophys. Fluid Dyn., 12, 73
Gizon L., 2004, Sol. Phys., 224, 217
Gizon L., Birch A. C., 2005, Living Rev. Sol. Phys., 2, 6. Online article: cited 9/01/2006, http://www.livingreviews.org/lrsp-2005-6
Hurlburt N. E., Rucklidge A. M., 2000, MNRAS, 314, 793
Hurlburt N. E., Matthews P. C., Rucklidge A. M., 2000, Sol. Phys., 192, 109
Jones C. A., Moore D. R., Weiss N. O., 1976, J. Fluid Mech., 73, 353
Knölker M., Schüssler M., 1988, A&A, 202, 275
Leka K. D., Steiner O., 2001, ApJ, 552, 354
Proctor M. R. E., Weiss N. O., 1982, Rep. Prog. Phys., 45, 1317
Sankarasubramanian K., Rimmele T., 2003, ApJ, 598, 689
Schlichenmaier R., 2002, Astron. Nachr., 323, 303
Schüssler M., Rempel M., 2005, A&A, 441, 337
Sobotka M., 2003, Astron. Nachr., 324, 369
Stix M., 2002, The Sun: An Introduction, 2nd edn. Astronomy & Astrophysics Library, Springer-Verlag, Berlin
Thomas J. H., Weiss N. O., 2004, ARA&A, 42, 517
Tildesley M. J., Weiss N. O., 2004, MNRAS, 350, 657
Tong C. H., 2005, Phil. Trans. R. Soc. A, 363, 2761
Weiss N. O., 2002, Astron. Nachr., 323, 371
Weiss N. O., Brownjohn D. P., Hurlburt N. E., Proctor M. R. E., 1990, MNRAS, 245, 434
Weiss N. O., Thomas J. H., Brummell N. H., Tobias S. M., 2004, ApJ, 600, 1073

This paper has been typeset from a TEX/LATEX file prepared by the author.